Analysis of GaN-based HEMTs operating as RF detectors over a wide temperature range

G. Paz-Martínez, I. Íñiguez de la Torre, H. Sánchez-Martín, T. González *Senior Member, IEEE* and J. Mateos *Member, IEEE*

***Abstract*— This paper presents an analysis of detection in the microwave region with AlGaN/GaN high-electron mobility transistors in terms of the key figures of merit: responsivity (both with voltage- and current-mode detection schemes) and noise equivalent power, in the temperature range between 20 and 400 K. Transistors with three different gates lengths (75, 150 and 250 nm) have been measured and favorably compared with a simple quasi-static model extracted from the DC curves, which is able to reproduce the zero-bias experiments at 1 GHz in the entire gate-bias sweep and operating temperature range. Such model allows to explain the detection experiments performed both with the devices operating in zero-current or zero-voltage conditions, and demonstrates that the bowing coefficient of the I_D-V_{DS} curves is the parameter which determines the performances of the devices as RF detectors. The voltage responsivity (in V/W) increases when the gate bias approaches the threshold voltage, but shows different behaviors in subthreshold conditions. Depending on whether the zero-current bias point is near zero drain voltage (for leaky devices, when the channel is not well pinched-off due to the short gate or to the conduction through the buffer at low temperature) or shifted to the point where third quadrant conduction starts (for well-behaved devices), the responsivity presents a decrease or an approximately constant value, respectively. On the other hand, when the detector is biased, the curves of current responsivity (in A/W) show a characteristic bell-shape with a maximum which is approximately the same for all tested devices and hardly depends on the gate bias (it is only shifted to different drain bias points).**

***Index Terms*— RF detection, zero-bias detector, GaN HEMTs, quasi-static model.**

I. INTRODUCTION

THE recent advances in transistor technology using narrow-bandgap high-mobility semiconductors have made possible to reach the milestone of THz amplification with a 25-nm InP high electron mobility transistor (HEMT) [1]. On the other hand, widebandgap-based transistors such as GaN HEMTs have desirable electrical characteristics for high-power high-temperature operation at moderately high frequencies [2].

In the last years different types of Field Effect Transistors (FETs) have been used as RF and THz detectors. Indeed, HEMTs are able to detect RF signals with frequencies much above their cutoff for amplification (described by their commonly used figures of merit f_t and f_{max}). Even if there is still controversy about the physical origin of such detection mechanism (plasmonic or thermoelectric effects can play a role [3]–[16]), practical THz detection is feasible with GaN HEMTs despite their lower cutoff frequencies with respect to faster InP-based devices. Wide bandgap semiconductors have the advantage of improved robustness and the possibility for high-power high-temperature operation, which may allow for applications such as ultrahigh-power RF detection or wireless power transmission [17].

In FET-based RF detectors operating in the voltage-mode scheme (with open-circuited output), the best noise equivalent power (NEP) is found when V_{GS} is just above the threshold bias value (V_{th}) [18], [19], but the maximum value of responsivity appears in the subthreshold region [19]–[21]. This operation region has attracted some attention in the literature and models have been proposed, some based on self-mixing square law detectors [20], [22]–[25] and plasma wave theory [21], [26]. Interestingly, in the current-mode detection scheme (with short-circuited output, best suited for fast operation), the results presented in the literature show that the responsivity vanishes for $V_{GS}<V_{th}$ [16], [22]. In practical cases (which are neither voltage- nor current-mode operation), the impedance of the readout system has also an effect in the value of the responsivity, diminishing as the load resistance decreases [18], [21], [23].

Even if zero-bias operation leads to optimum low noise operation and allows one to get rid of self-heating effects, in this work we present a complete study of both zero-bias and biased RF detection with AlGaN/GaN HEMTs in a wide range of temperature (20-400 K). Drain-coupled RF injection in both current- and voltage-mode detection schemes will be employed in our experiments and the results will be interpreted in terms of the non-linearity of the I_D-V_{DS} curves (low-frequency resistive mixing mechanism) [27]. For that sake, a simple quasi static (QS) model [27], [28] will be used, able to capture all the features of the RF responsivity in all of the operation conditions just by analyzing the static I_D-V_{DS} characteristics at the corresponding operating point. In Section II the devices under test (DUT) and the experimental set-up are described. The QS model is explained in Section III and afterwards, in Section III,

Manuscript received ¿? 2022; revised ¿? 2022; accepted ¿? 2022. Date of publication ¿? 2022; date of current version ¿? 2022.This work has been partially supported through grant PID2020-115842RB-I00 funded by MCIN/AEI/10.13039/501100011033 and Junta de Castilla and León and FEDER through project SA254P18.

G. Paz-Martínez, I. Íñiguez de la Torrre, H. Sánchez-Martín, T. González and J. Mateos, are with the Applied Physics Department, and USAL-NANOLAB, Universidad de Salamanca, 37008 Salamanca, Spain.

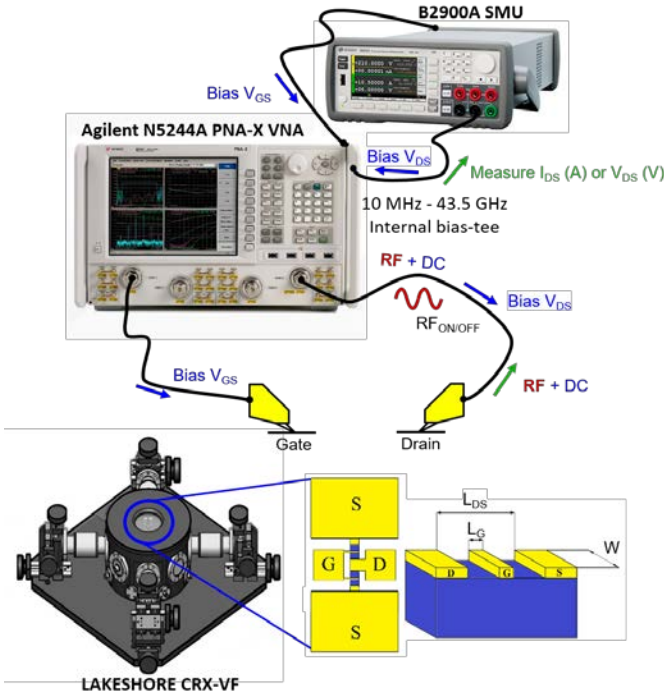

Fig. 1. Sketch of the measurement setup. The cryogenic probe station is used to connect the transistor to the VNA and the SMU. Ground-signal-ground probes allow to access the device. All the system is controlled by means of a LabView code accounting for the losses of the cables and tips (by means of a SOLT calibration) to ensure that a RF power of -15 dBm reaches the reference plane of the transistor.

the experimental and modeled results are presented and the origin of the behavior of the RF detection in the different operation modes is discussed. Finally, the main conclusions of our work are drawn in Section V.

II. Device under test, experimental setup

In this work, we focus our study on AlGaN/GaN HEMTs grown on a high resistivity silicon substrate whose details are provided in [29]–[31]. The characterized devices have a drain-to-source distance L_{DS}=2.5 µm, a width of W=2×25 µm and three different gate lengths L_G=75 nm, 150 nm and 250 nm. For the measurements, see Figure 1, the DUTs are placed inside a LakeShore CRX-VF cryogenic probe station, and are on-wafer connected by means of GSG RF probes to a VNA Keysight N5244A, used as RF power source (which is injected to the drain contact). A two-channel SMU B2902A allows both biasing the device and record the output voltage/current detected at the drain terminal. One channel of the SMU is connected to the gate and the other to the drain terminal, in this case through the internal bias-tee of the VNA, making possible combining the RF input and the DC bias. The selected operating temperatures are 20, 100, 200, 300 and 400 K.

Two different zero-bias detection schemes can be employed, zero-current voltage-mode (ZC), where drain terminal is open-circuited and its voltage is measured, or zero-voltage current-mode (ZV) when drain terminal is short-circuited and its current is measured. The responsivity in ZV conditions is the ratio $\beta_I^{ZV} = \Delta I_D / P_{in}$, where ΔI_D is the DC drain current response to the RF input signal whose input power is P_{in}. Conversely, in ZC conditions, $\beta_V^{ZC} = \Delta V_{DS} / P_{in}$ where ΔV_{DS} is the DC drain voltage shift caused by the RF excitation.

The most important figure of merit for detectors is the noise equivalent power (NEP), which indicates their sensitivity for detecting low-power signals and is defined as the relation between the noise amplitude and the responsivity (both under current- or voltage-mode operation):

$$NEP = V_n/\beta_V = I_n/\beta_I \text{ , in W/}\sqrt{Hz} \tag{1}$$

being V_n and I_n the voltage- and current-noise amplitudes, respectively. Under ZC or ZV conditions, we can assume that V_n and I_n take the equilibrium values given by the Nyquist theorem, so that the value of the *NEP* is:

$$NEP^{ZC} = \sqrt{(4k_B T R_D^{ZC})}/\beta_V^{ZC}, \tag{2}$$

$$NEP^{ZV} = \sqrt{(4k_B T / R_D^{ZV})}/\beta_I^{ZV}, \tag{3}$$

being R_D^{ZC} and R_D^{ZV} the drain resistance at $I_D = 0$ and $V_{DS} = 0$, respectively, k_B the Boltzmann constant and T the lattice temperature. The only possible difference between NEP^{ZC} and NEP^{ZV} is just associated to the fact that ZC and ZV bias points may not be the same, as we will see later in the results section.

When the detector is biased (and neither ZC nor ZV conditions apply), excess noise is generated, so that the noise power should be measured in order to determine the exact value of the *NEP*.

III. Quasi-static model

Based on the static I_D-V_{DS} curves, an analytical quasi-static (QS) model is able to predict the RF responsivity (β_{QS}) at low frequency of FETs based on the differential drain-source resistance, R_D, and the bowing coefficient γ which can be extracted from the $I_D(V_{DS})$ dependence as:

$$R_D = \left(\frac{\partial V_{DS}}{\partial I_D}\right) = \left(\frac{\partial I_D}{\partial V_{DS}}\right)^{-1}, \tag{4}$$

$$\gamma = \frac{\frac{\partial^2 I_D}{\partial V_{DS}^2}}{\frac{\partial I_D}{\partial V_{DS}}} = \frac{\partial^2 I_D}{\partial V_{DS}^2} R_D \text{ (in V}^{-1}\text{ units)}, \tag{5}$$

We have to remark that non-quasi-static mechanisms such as self-heating or trapping effects [32]–[34] may lead to a low-frequency dispersion of the responsivity of the devices (as happens in nanometric-width diodes [35]), and originate discrepancies between the predictions of the QS model and the experimental results at GHz frequencies. In the case of the transistors studied here, first, self-heating is almost negligible (mainly in zero-bias conditions, but also when biasing the devices, since the dissipated power is very low). Self-heating effects in the same transistors were previously studied by means of Monte-Carlo simulations and pulsed I_D-V_{DS} characterization in [31]. Moreover, low frequency dispersion was observed in virgin devices [36] but disappeared after biasing the transistors. Therefore, an almost perfect coincidence between the between the QS model predictions taking as a base the DC I_D-V_{DS} curves and the responsivities measured at 1 GHz is found.

In case trapping or heating effects were significant in the operation of the transistors as RF detectors, the QS model would account for them all since they could be evidenced by

means of pulsed I_D-V_{DS} measurements. By measuring the I_D-V_{DS} curves with different pulse widths, the frequency dependence of R_D and γ would be obtained, and by applying the proposed QS model (which is still valid for linking the so obtained I_D-V_{DS} and the RF detection) the possible frequency dispersion of the detection would be straightforwardly obtained.

III.1 *Current-mode detection*

The QS model [27], [28], [37] is based on the second order Taylor series expansion of the current as a function of the voltage,

$$I_D \approx I_{D0} + \Delta V_{DS}\frac{\partial I_D}{\partial V_{DS}} + \frac{1}{2}\Delta V_{DS}^2\frac{\partial^2 I_D}{\partial V_{DS}^2}, \quad (6)$$

where $I_{D0} = I_D(V_{DS0})$ is the DC bias term, $\Delta V_{DS} = V_{DS}$-V_{DS0} with $V_{DS}(t) = V_{DS0} + V_{RF}\cos(2\pi f t)$ the harmonic RF excitation with frequency f and amplitude V_{RF} sufficiently small so that higher order terms can be neglected. The derivatives have to be evaluated around the bias point (I_{D0}, V_{DS0}). Because of the harmonic signal excitation, the time-dependent current can be obtained from eq. (6) as:

$$I_D(t) \approx I_{D0} + V_{RF}\cos(2\pi f t)\frac{\partial I_D}{\partial V_{DS}} + \frac{1}{4}V_{RF}^2[1+\cos(4\pi f t)]\frac{\partial^2 I_D}{\partial V_{DS}^2}. \quad (7)$$

Therefore, the detected current ΔI_D, obtained as the difference between the average value of $I_D(t) = \overline{I_D(t)}$ and the drain current without RF excitation I_{D0} is:

$$\Delta I_D = \overline{I_D(t)} - I_{D0} \approx \frac{1}{4}V_{RF}^2\frac{\partial^2 I_D}{\partial V_{DS}^2}. \quad (8)$$

Since the RF responsivity, β, is defined as the ratio between the output signal and the input power, in order to evaluate the value of the current-mode responsivity $\beta_I = \Delta I_D / P_{in}$ (in A/W units), one must first take into account that the RF power dissipated by the detector is:

$$P_{in} = \frac{1}{T}\int_0^T [I_D(t) - I_{D0}][V_{DS}(t) - V_{DS0}]dt = \frac{1}{2}\frac{V_{RF}^2}{R_D}. \quad (9)$$

Using eqs. (2), (5) and (6), the optimum value of β_I, without considering the impedance mismatch between the RF source and the detector, can be obtained with this QS model as:

$$\beta_{I,opt}^{QS} = \frac{1}{2}\frac{\partial^2 I_D}{\partial V_{DS}^2}R_D = \frac{1}{2}\gamma\,. \quad (10)$$

III.2 *Voltage-mode detection*

The same reasoning can be applied to the voltage-mode detection if a RF harmonic current excitation around the bias point (I_{D0}, V_{DS0}) is considered, $I_D(t) = I_{D0} + I_{RF}\cos(2\pi f t)$. In this case the output signal obtained is the drain bias shift $\Delta V_{DS} = \overline{V_{DS}(t)} - V_{DS0}$, and the voltage-mode responsivity is obtained as $\beta_V = \Delta V_{DS}/P_{in}$ (in V/W units). For that sake one must start with the Taylor expansion of the reciprocal expression of the I_D-V_{DS} curves $V_{DS}(I_D)$, so that an expression similar to eq. (8) is obtained:

$$\Delta V_{DS} = \overline{V_{DS}(t)} - V_{DS0} \approx \frac{1}{4}I_{RF}^2\frac{\partial^2 V_{DS}}{\partial I_D^2}. \quad (11)$$

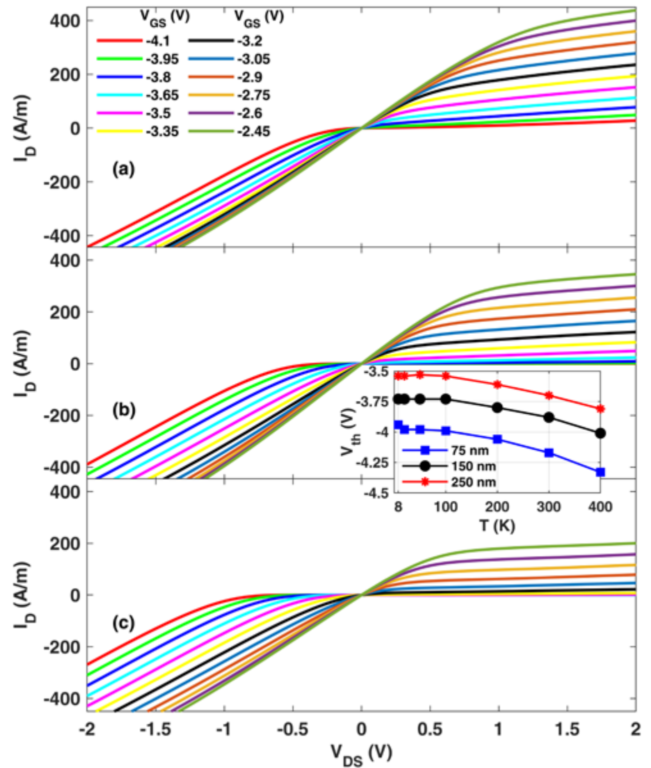

Fig. 2. $I_D - V_{DS}$ output characteristics for the HEMTs with (a) L_G=75 nm, (b) L_G=150 nm (c) L_G=250 nm at 300 K. The region of negative values of V_{DS} shows the onset of the TQC when $V_{DS} < V_{GS} - V_{th}$. The Inset in (b) shows the V_{th} vs. T dependence for the different gate lengths.

and knowing that in this case the RF power can be calculated as $P_{in} = \frac{1}{2}I_{RF}^2 R_D$, the optimum voltage responsivity $\beta_{V,opt}^{QS}$ can be computed as:

$$\beta_{V,opt}^{QS} = \frac{\Delta V_{DS}}{P_{in}} = \frac{\frac{1}{4}I_{RF}^2\left(\frac{\partial^2 V_{DS}}{\partial I_D^2}\right)}{\frac{1}{2}I_{RF}^2 R_D} = \frac{1}{2}\left(\frac{\partial^2 V_{DS}}{\partial I_D^2}\right)R_D^{-1}. \quad (12)$$

and since

$$\frac{\partial^2 V_{DS}}{\partial I_D^2} = \frac{\partial}{\partial I_D}\left(\frac{\partial V_{DS}}{\partial I_D}\right) = \frac{\partial}{\partial I_D}\left(\frac{\partial I_D}{\partial V_{DS}}\right)^{-1} = -\frac{\frac{\partial}{\partial I_D}\left(\frac{\partial I_D}{\partial V_{DS}}\right)}{\left(\frac{\partial I_D}{\partial V_{DS}}\right)^2}$$

$$= -\frac{\frac{\partial V_{DS}}{\partial I_D}\times\frac{\partial}{\partial V_{DS}}\left(\frac{\partial I_D}{\partial V_{DS}}\right)}{\left(\frac{\partial I_D}{\partial V_{DS}}\right)^2} = -\frac{\frac{\partial^2 I_D}{\partial V_{DS}^2}}{\left(\frac{\partial I_D}{\partial V_{DS}}\right)^3} = -\frac{\partial^2 I_D}{\partial V_{DS}^2}R_D^3, \quad (13)$$

one can easily obtain the value of the voltage responsivity using the definition of γ given in eq. (5), as:

$$\beta_{V,opt}^{QS} = -\frac{1}{2}\left(\frac{\partial^2 I_D}{\partial V_{DS}^2}\right)R_D^2 = -\frac{1}{2}\gamma R_D = -\beta_{I,opt}^{QS}R_D\,. \quad (14)$$

Therefore, an often overlooked property of RF detectors is demonstrated, (i) current- and voltage-mode responsivities have opposite sign and, (ii) as expected, the rate of their modules is R_D.

III.3 *Impedance Mismatch*

In order to obtain the practical value of the responsivities of a given detector, the mismatch between the impedance of the device (Z_d, which can be assumed to be equal to R_D at low

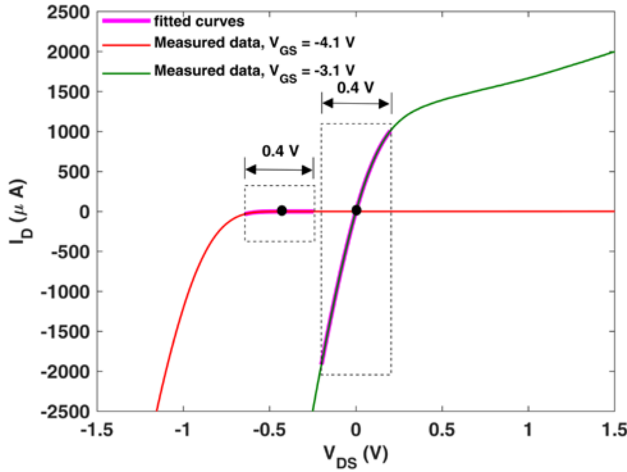

Fig. 3. $I_D - V_{DS}$ output characteristics for V_{GS}= -4.1 V and - 3.1 V for L_G=250 nm at 300 K. At each Q-point a polynomial fitting is made in a window of $\Delta V_{DS}=0.4$ V.

frequency) and the source (Z_s) should be accounted for. So that, the unmatched responsivity with a standard 50 Ω source is

$$\beta_{I,50}^{QS} = \frac{1}{2}\gamma(1-|\Gamma|^2) \tag{15}$$

$$\beta_{V,50}^{QS} = -\frac{1}{2}R_D\gamma(1-|\Gamma|^2)\ , \tag{16}$$

where $\Gamma=(Z_d-Z_s)/(Z_d+Z_s)$ is the reflection coefficient of the RF input signal due to the impedance mismatch between the source and the detector, being Z_s=50 Ω.

In the strongly mismatched case, when $Z_s \ll R_D$ (as happens in our devices when V_{GS} approaches V_{th}) $|\Gamma|\approx 1$, and $(1-|\Gamma|^2)\approx 4Z_s/R_D$, so that $\beta_{I,50}^{QS}$ vanishes and the voltage responsivity is independent of the device impedance taking a value of

$$\beta_{V,50}^{QS} \approx -2Z_s\gamma = -100\gamma. \tag{17}$$

IV. Results and Discussion

Figure 2 shows the $I_D - V_{DS}$ characteristics for the GaN HEMTs with gate lengths L_G=75, 150 and 250 nm, including the negative V_{DS} region, which plays a key role for drain-injected RF power detection. Indeed, the third quadrant conduction (TQC) region (typical of FETs) is clearly observed. The TQC region appears as a consequence of the symmetry of the device [37]–[39], so that the conduction condition for the gate voltage when a drain bias is applied ($V_{GD} = V_{GS} - V_{DS} > V_{th}$) is fulfilled when V_{DS} takes negative values below $V_{GS} - V_{th}$. For FETs operating as RF detectors, TQC has an important influence, particularly in subthreshold conditions ($V_{GS} < V_{th}$) as we will show in this study. The $I_D - V_{DS}$ curves at low temperatures do not show any kink or other non-ideal behavior in the drain-bias range under analysis (see the results shown in [37]).

The value of V_{th} is calculated as the V_{GS} value where the extrapolation of the linear region of the curve $\sqrt{I_{DS}} - V_{GS}$ intercept the V_{GS} axis for V_{DS}=0.1 V (approximately where the devices operate for ZC or ZV detection). The inset of Figure 2 (b) presents the values obtained for V_{th} as a function of temperature. As expected, V_{th} is more negative as the gate length is reduced due to short channel effects. Moreover, regardless of the gate length, it is constant with temperature below 100 K and then slightly decreases with increasing temperature.

In order to understand correctly the detection results that will be shown later, a key point to bear in mind is the location the static operation point (Q-point) of the HEMTs, since it will determine their performances. By applying the QS model to the measured DC characteristics around the Q-point we will have a precise estimation of the RF detection figures of merit of the transistor at low frequency. Figure 3 shows two selected $I_D - V_{DS}$ curves from Figure 2(c) for V_{GS}= -4.1 V and -3.1 V, corresponding to subthreshold and above-threshold conditions, respectively (V_{th} ≈-3.7 V for this 250-nm-gate HEMT at 300 K). The parameters of the QS model are obtained at each Q-point of the measured DC curves trough a polynomial fitting in a window of ΔV_{DS}=0.4 V (see Figure 3) centered at a specific point in the curve fixed by its I_D or V_{DS} value depending on whether voltage- or current-mode detection is used. In that way, the channel resistance, bowing coefficient and the current- and voltage-mode responsivities (and also the *NEP*, if in equilibrium conditions) can be obtained as a function of the bias. In Figure 3 the Q-points represented correspond to the zero-I_D bias point, which, surprisingly shifts to negative values of V_{DS} when V_{GS} enters into the subthreshold region. This is so because there is always a small positive I_D leakage current which flows out of the drain terminal even if V_{DS}=0, due to the non-zero value of the gate leakage current (with $I_D \approx |I_G|/2$, since half of the gate flows out to the source terminal, see [37]). As a consequence, a negative V_{DS} is created when the bias condition I_D=0 is maintained. This is especially evident well in subthreshold conditions ($V_{GS} < V_{th}$), because the Q-point is significantly shifted to the (negative) V_{DS} value corresponding approximately to the onset of the TQC, $V_{DS} \approx V_{GS} - V_{th}$ (in the case of no significant buffer leakage [37]). Note the quite

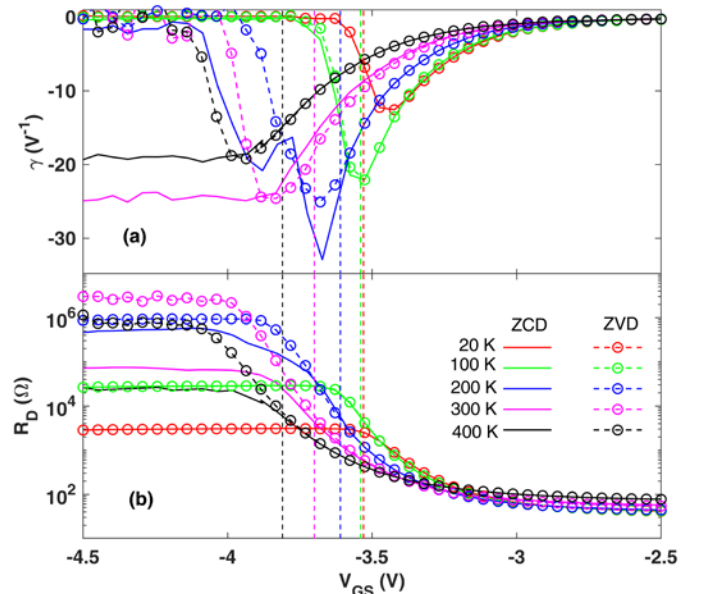

Fig. 4. (a) Bowing coefficient, γ, and (b) R_D in ZC (solid lines) and ZV (symbols, dashed lines) conditions for the HEMT with L_G=250 nm. The values are obtained by applying the QS model to the DC measurements of the I_D-V_{DS} curves of the device in the temperature range 20-400 K. The vertical dashed lines indicate the value of V_{th} for each *T*.

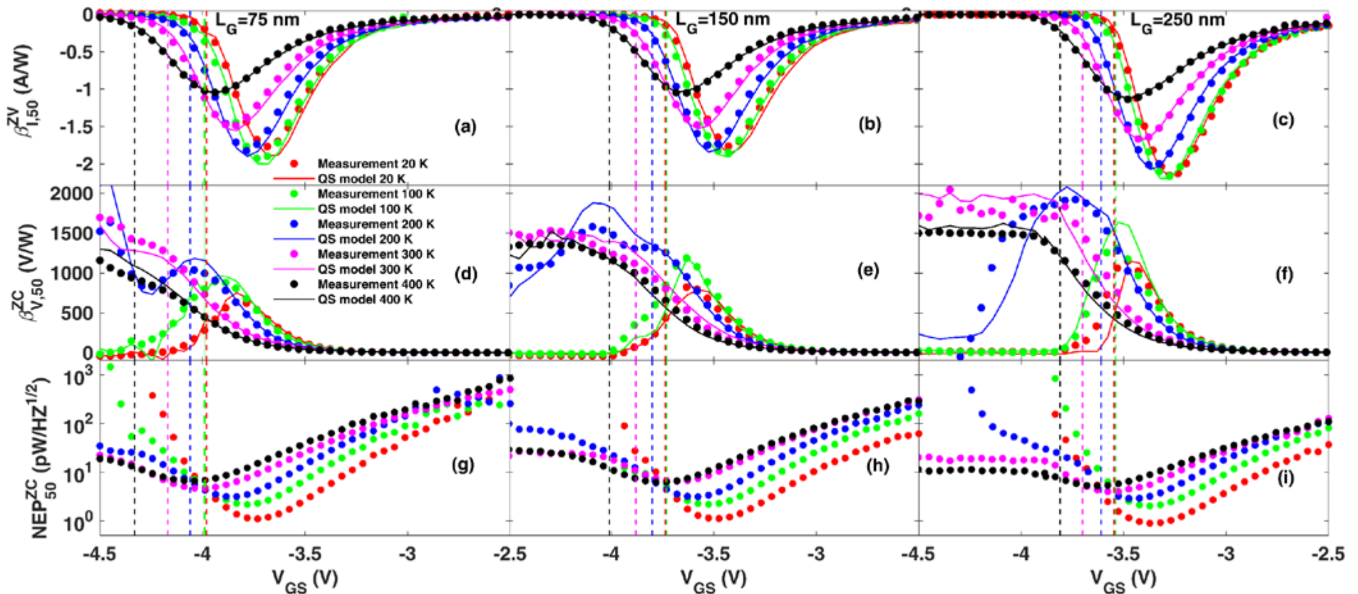

Fig. 5. Comparison of the zero-bias responsivity measured at 1 GHz (symbols) and calculated with the QS model (lines) as a function of the gate bias in the 20-400 K temperature range. (a), (b) and (c) show the current-mode ZV results and (d), (e) and (f) the voltage-mode ZC results. The value of the NEP^{ZC}_{50} extracted from eq. (11) is plotted in (g), (h) and (i). (a), (d) and (g) correspond to a HEMT with L_G=75 nm, (b), (e) and (h) to L_G=150 nm and (c), (f) and (i) to L_G=250 nm. The dashed vertical lines indicated the values of V_{th} for each T. The experiments were made with a small input RF power of P_{in}= -15 dBm.

different shape of the $I_D - V_{DS}$ curve around the Q-point when this is shifted to negative values of V_{DS}.

In order to evidence the effect of the Q-point shift on the detection performances, Figure 4 shows the values of γ and R_D for L_g=250 nm, both at zero-I_D (ZC) and zero-V_{DS} (ZV) conditions, obtained using the previously explained QS model. For T≤100 K, the value of γ is similar in ZC and ZV conditions, with a maximum value for V_{GS} around (or slightly below) V_{th}, dropping to zero both in open channel and subthreshold regions. However, for higher T, the curves start to diverge when V_{GS}<V_{th}: γ goes to zero in ZV but remains nearly constant at its maximum value in ZC. This happens because of the previously explained shift of the Q-point in ZC with respect to ZV conditions, which takes place only at T>100 K. As explained in [37], at low T, the ionization level of the buffer acceptors decreases (C atoms are present in our samples in a concentration of about 10^{17} cm^{-3} leading to a semi-insulating GaN buffer), so that a significant drain leakage current flows through the buffer. In those conditions, a small drain voltage induces a significant negative drain leakage current, which compensates the positive gate contribution (without the need of TQC), and therefore the ZC and ZV Q-points are both located at the origin of the graph (the zero-I_D point is nearly at V_{DS}=0).

On the other hand, R_D increases when decreasing V_{GS} and saturates when entering the subthreshold region, Figure 4(b), with a value which strongly depends on T. Indeed, the value of R_D in subthreshold conditions first increases when lowering T and then sharply decreases as a consequence of the drain current leakage through the buffer (associated to non-ionized acceptors) previously discussed. And, since the values of R_D when V_{GS}<V_{th} are lowered by the shift of the Q-point in ZC conditions at T>100 K, their maximum values (~MΩ) are observed at 200 K in ZC and 300 K in ZV conditions, a similar behavior to that of γ.

IV.1 *Zero-Bias detection*

Figure 5 shows the excellent agreement found between the RF detection measurements made at 1 GHz (with a small input RF power of P_{in}= -15 dBm) and the results obtained with the QS model for the three devices with L_G=75, 150 and 250 nm (in a wide temperature range of 20-400 K). Remarkably, only a weak dependence on L_G is observed.

Regarding current-mode ZV detection, the responsivity always exhibits a bell-shaped behavior, vanishing in subthreshold conditions, as expected from eq. (15), due to the strong impedance mismatch. This also makes the maximum of $\beta^{ZV}_{I,50}$ to be found for V_{GS} around 0.2-0.3 V above V_{th} in all the cases, shifted to the right with respect to the maximum of γ, Figure 4(a), due to the influence of the $(1 - |\Gamma|^2)$ factor which approaches zero when V_{GS} approaches V_{th}.

The maximum value of $\beta^{ZV}_{I,50}$ increases as T decreases due to the enhancement of γ observed in Figure 4(a), but only down to a certain T when the pinch-off of the device starts to be degraded, as observed in Figure 6(b), where the values of the main detection figures of merit for the optimum V_{GS} are presented (in absolute value). However, even if the maximum value of γ is obtained at T=200 K, the best current responsivity is found at the lowest T. This happens because as T decreases a lower γ is compensated with a better impedance matching (R_D is lower, below the kΩ range, due to a higher electron mobility) at around V_{GS}=V_{th}+0.2 V, where the maximum $\beta^{ZV}_{I,50}$ is obtained, see Figure 4(b).

Regarding ZC detection, Figures 5(d)-(f), the values of $\beta^{ZC}_{V,50}$ follow the two different trends (depending on the temperature range) observed for γ in Figure 4(a): the responsivity reaches its maximum near V_{GS}=V_{th} and then drops in subthreshold conditions for T≤100 K, while for T>100 K $\beta^{ZC}_{V,50}$ remains constant at around its maximum. In this case, contrary to what

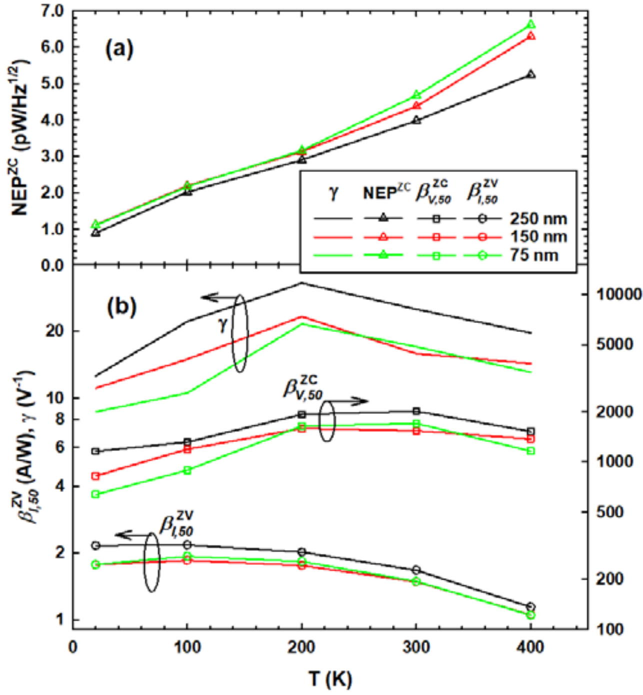

Fig. 6. Optimum values of the zero-bias detection figures of merit as a function of *T*: (a) NEP^{ZC}, and (b) $\beta^{ZV}_{I,50}$, $\beta^{ZC}_{V,50}$, and γ, for the devices with L_G=75, 150 and 250 nm.

found for $\beta^{ZV}_{I,50}$, the maximum value of $\beta^{ZC}_{V,50}$ decreases when lowering the temperature, which is best in the 200-300 K range (when the pinch-off behavior of the transistors is optimum), since it is also degraded at high *T* [19]. As observed in Figure 6(b), this happens because $\beta^{ZC}_{V,50}$ can be approximated by the value given by eq. (17), -100γ (its maximum is always found in conditions of strong mismatch), so that its dependence with *T* is much the same as that of γ.

Regarding the noise equivalent power NEP^{ZC} calculated with eq. (2), Figs. 5(g), (h) and (i), the optimum values are obtained, regardless of L_G, approximately for the same V_{GS} as the maximum of $\beta^{ZV}_{I,50}$ (around V_{th}+0.2 V), again because the higher resistance degrades the *NEP*. We have chosen to represent the value of NEP^{ZC}, but the values of NEP^{ZV} are nearly the same above threshold, so that the optimum values of the NEP^{ZC} and NEP^{ZV} coincide. Figure 6(a) shows that the *NEP* of our devices increases with *T*, taking very competitive values [19], around 1 pW/√Hz at 20 K rising to around 5 pW/√Hz at 400 K, and are (slightly) better for L_G=250 nm.

Only a slight dependence of the zero-bias detection figures of merit on L_G is observed in Fig. 6. Since a better pinch-off behavior leads to an enhanced non-linearity, a slight degradation when reducing L_G is observed due to short-channel effects, thus decreasing γ and consequently $\beta^{ZC}_{V,50}$, $\beta^{ZV}_{I,50}$ and *NEP* for the shortest L_G=75 nm. The other side of the coin is that, even if a longer gate improves the low-frequency detection, it reduces the cutoff frequency of the resistive mixing detection mechanism, so that a tradeoff between both of them must be chosen.

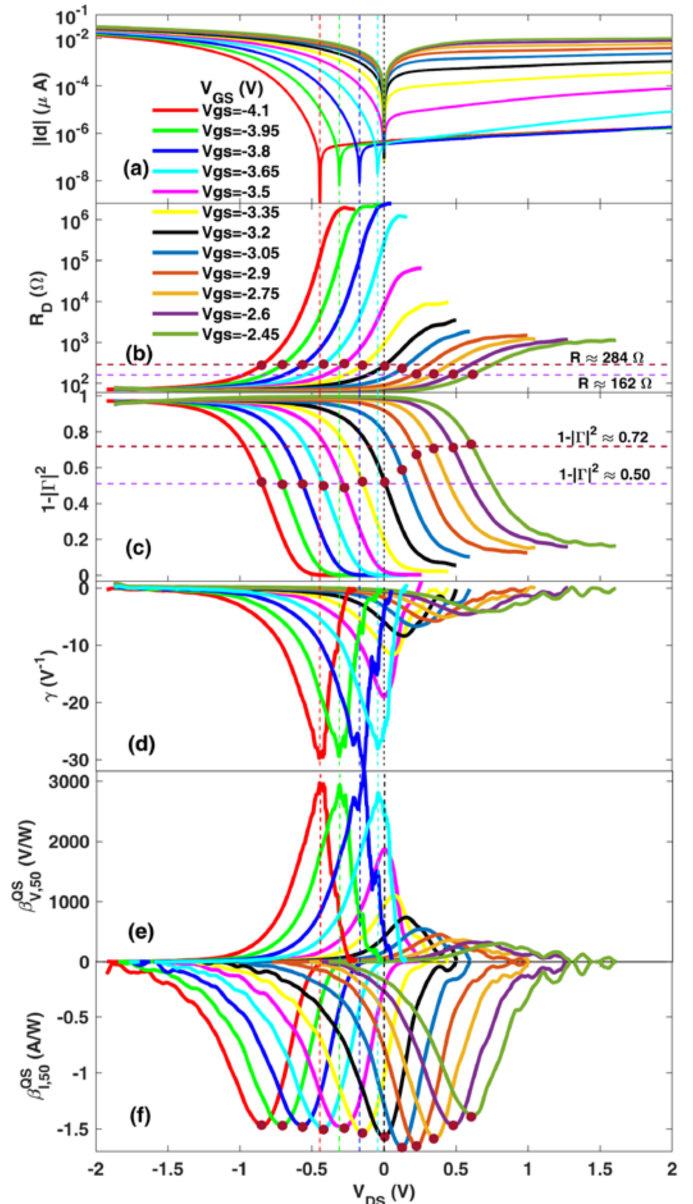

Fig. 7. (a) $I_D - V_{DS}$ characteristics in log scale. The ZC voltage (V_{DS} for which $I_D = 0$) is indicated by the vertical dashed lines. (b) shows the channel resistance R_D (c) the impedance mismatch factor $(1 - |\Gamma|^2)$, (d) the bowing coefficient γ, (e) the current responsivity $\beta^{QS}_{I,50}$, and (f) the voltage responsivity $\beta^{QS}_{V,50}$, all of them calculated with the QS model as a function of V_{DS} for several values of V_{GS}. Circles in (b), (c) and (f) indicate the points (for each V_{GS}) where the maximum current responsivity is obtained. L_G=250 nm and *T*=300K.

IV.2 *Biased detection*

Even though zero-bias operation is preferable in terms of *NEP* (no excess noise is generated), biased detection allows to improve the responsivity by purposely locating the Q-point where the $I_D - V_{DS}$ curves exhibit their optimum non-linear behavior [40]–[42]. Figure 7 shows the different figures of merit calculated with the QS model for L_G=250 nm at T =300 K as a function of V_{DS} for different V_{GS}. Figure 7(a) shows the same $I_D - V_{DS}$ curves of Figure 2(c), but this time representing $|I_D|$ in log scale, so that the ZC point (I_D=0) is

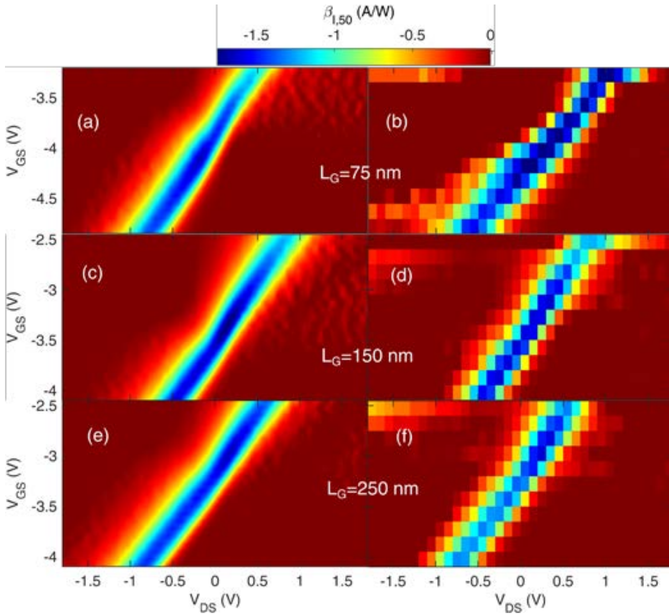

Fig. 8. Color maps of $\beta_{I,50}(V_{DS})$ as a function of V_{GS} at T =300 K, obtained with (a), (c) and (e) the QS model and (b), (d) and (f) measured with P_{in} =-15 dBm at 1 GHz. (a) and (b) L_G=75 nm (V_{th} ≈-4.2 V), (c) and (d) L_G=150 nm (V_{th} ≈-3.9 V) and (e) and (f) L_G=250 nm (V_{th} ≈-3.7 V). The horizontal dashed lines indicate the values of the threshold voltages.

clearly visible. The drain voltage corresponding to the zero-current point (indicated by the vertical dashed lines for each V_{GS}), shifts to the left in subthreshold conditions ($V_{GS} < V_{th}$, with $V_{th} \approx -3.7$ V in this case). In our previous work [37] we showed that the presence of a drain leakage current and its competition with TQC fixes the zero-crossing of I_D in subthreshold. The lower the drain leakage the stronger the phenomenon is, so that short gate lengths (giving rise to short-channel effects) and low temperatures (buffer acceptor ionization level decreases) significantly suppress this voltage shift of the ZC point.

Figure 7(b) shows the values of the differential resistance, R_D, taking a minimum value of 72 Ω in open channel and TQC conditions, sharply increasing with V_{DS}, reaching the MΩ range when V_{GS} is in subthreshold or up to some kΩ when saturation in the 1st quadrant is attained. Conversely, the mismatch factor $(1-|\Gamma|^2)$ calculated from the previous values of R_D, Figure 7(c), goes, when V_{DS} is increased, from almost perfect matching (97%), to almost 0 in subthreshold or to around 20% for high V_{GS} (open channel), with the curves shifted to higher V_{DS} when V_{GS} is raised.

It must be noted that the impedance mismatch of the devices with the 50 Ω source can be improved by increasing the gate width of the transistors, which decreases their resistance, thus allowing to strongly enhance their current-mode responsivity [43]. However, the voltage-mode responsivity is not improved because the lower input losses are compensated by the smaller resistance of the transistor, see eq. (16). As a consequence, the maximum voltage responsivity is always near the constant value predicted by eq. (17), corresponding to the strongly-mismatched case, since it is obtained near pinch-off.

Regarding γ, Figure 7(d), in subthreshold conditions its maximum value is attained at the onset of the TQC, for the (negative) V_{DS} value corresponding to the ZC point. The dependence of γ on V_{DS} is similar while $V_{GS} < V_{th}$, reaching a similar minimum of about -30 V^{-1}, just with a shift of V_{DS} parallel to the V_{GS} increase. On the other hand, for $V_{GS} > V_{th}$ the maximum of γ decreases and appears for positive V_{DS} values (at the knee of the $I_D - V_{DS}$ curve, where the increase of R_D is less pronounced than for TQC), always shifting to higher V_{DS} as V_{GS} increases. This dependence of increase of γ allows to straightforwardly explain the values of the voltage responsivity $\beta_{V,50}^{QS}(I_D)$, Figure 7(e). First, the maximum values appear in the subthreshold region, where, regardless of V_{GS}, are around 3 kV/W, near the -100γ value expected from eq. (17) in strongly mismatched conditions. Note that the maximum of both γ and $\beta_{V,50}^{QS}(I_D)$ appears at the onset of the TQC, where R_D is in the kΩ range, Fig. 7(b). Second, for $V_{GS} > V_{th}$, γ and $\beta_{V,50}^{QS}(I_D)$ rapidly decrease, even if the mismatch is not as large as in subthreshold conditions.

On the other hand, the values of $\beta_{I,50}^{QS}(V_{DS})$ obtained with eq. (15), shown in Figure 7(f), always exhibit a bell shape for each given V_{GS}. However, even though γ sharply decreases for $V_{GS} > V_{th}$, in this case its decrease is completely compensated by the lower mismatch, so that the optimum $\beta_{I,50}^{QS}$ is around -1.5 A/W almost independently of V_{GS}, and even slightly increases just above V_{th}. The optimum V_{DS} bias point is indicated with circular symbols in Figures 7(b), (c) and (f), showing that in subthreshold the peak value for $\beta_{I,50}^{QS}(V_{DS})$ takes place around R_D ≈284 Ω (corresponding to a mismatch of about 50%). The reason why $\beta_{I,50}^{QS}$ slightly improves for $V_{GS} > V_{th}$ is the enhanced power matching (reaching about 72%). These dependences on V_{DS} and V_{GS} obtained by the QS model have been confirmed by the experiments shown in Figure 8, where the theoretical current responsivities in biased conditions are quite favorably compared with the measured values at 1 GHz for all the three different gate lengths at T=300 K. Remarkably, the maximum value of $\beta_{I,50}$ hardly depends on L_G, taking values of around -1.6 A/W.

Here it is necessary to remark that the analysis of biased detection made in this section is based on the measurements made on a different device from that presented in Figure 5. Even though they are similar devices, a certain variability in the fabrication process and the non-homogeneity of the epilayer characteristics induces variations on the pinch-off behaviour of the HEMTs, thus resulting in differences on the values of V_{th}, R_D, and, consequently, in γ and both β_V and β_I, which are linked as shown by eqs. (15) and (16). This leads to some slight discrepancies between the values shown in Figure 7 with respect to Figure 5, mainly regarding γ and β_V. However, the

qualitative analysis and conclusions extracted here for the HEMT with L_G=250 nm are general and valid also for the devices with L_G=150 nm and L_G=75 nm. It is also interesting to remark that the current responsivity $\beta_{I,50}$ has much smaller variability due to the fact that it goes to zero when approaching subthreshold conditions, so that its values are much less sensitive to the dissimilarities on the pinch-off behaviour of the devices.

The main result of this section is that the RF detection performances of the HEMTs cannot be improved by biasing the devices, neither in voltage-mode nor in current-mode operation. In voltage mode, the optimum V_{DS} is obtained by the spontaneous self-bias at the zero-current operation point (which provides the best non-linearity), while in current mode the maximum responsivity (which coincides with the optimum NEP) can be obtained with V_{DS}=0 by adequately choosing the V_{GS} value to around V_{th}+0.3 V.

V. Conclusions

The QS-model employed in this work is a simplistic and easy way to understand the RF detection performances at low frequencies (while the resistive mixing mechanism based on the non-linearity of the devices holds). In this work it has been applied to obtain the responsivity and NEP of GaN HEMTs operating as RF detectors both in current- and voltage-mode and in zero-bias and biased operation in a wide temperature range, correctly reproducing the experimental results.

There are marked differences between the two detection schemes. When the voltage responsivity is measured, the best response is presented at the ZC point. Under this detection mode scheme, if the transistor has a good pinch-off, the bias point is shifted to the V_{DS} corresponding to the onset of TQC, thus maintaining a high responsivity in subthreshold. On the other hand, leaky devices (due to short channel effects or non-ionized buffer acceptors at low T) have low voltage responsivity in subthreshold regime due to their linearity around the ZC point. Regarding the dependence with T, the maximum voltage responsivity is attained at intermediate temperatures, associated to an optimum non-linear behavior of the transistors. Conversely, when operating in current-mode, the responsivity is null in subthreshold conditions. A maximum value around 1.5-1.6 A/W is obtained for $V_{GS} \approx V_{th}$+0.3 V at T=300 K, increasing to about 2 A/W at low T, almost independently of the gate length.

Finally, no improvement of the RF detection performances can be obtained by means of drain biasing, the optimum zero-bias detection conditions can be achieved just by choosing the adequate value of V_{GS}.

Acknowledgements

The authors would like to thank V. Hoel and Y. Cordier for providing the devices measured in this work.

References

[1] X. Mei *et al.*, «First Demonstration of Amplification at 1 THz Using 25-nm InP High Electron Mobility Transistor Process», *IEEE Electron Device Lett.*, vol. 36, n.º 4, pp. 327-329, abr. 2015, doi: 10.1109/LED.2015.2407193.

[2] U. K. Mishra, P. Parikh, y Yi-Feng Wu, «AlGaN/GaN HEMTs-an overview of device operation and applications», *Proc. IEEE*, vol. 90, n.º 6, pp. 1022-1031, jun. 2002, doi: 10.1109/JPROC.2002.1021567.

[3] W. Knap *et al.*, «Plasma wave detection of sub-terahertz and terahertz radiation by silicon field-effect transistors», *Appl. Phys. Lett.*, vol. 85, n.º 4, pp. 675-677, jul. 2004, doi: 10.1063/1.1775034.

[4] S. Kang, P. J. Burke, L. N. Pfeiffer, y K. W. West, «Resonant frequency response of plasma wave detectors», *Appl. Phys. Lett.*, vol. 89, n.º 21, p. 213512, nov. 2006, doi: 10.1063/1.2393023.

[5] A. El Fatimy *et al.*, «Resonant and voltage-tunable terahertz detection in InGaAs⁄InP nanometer transistors», *Appl. Phys. Lett.*, vol. 89, n.º 13, p. 131926, sep. 2006, doi: 10.1063/1.2358816.

[6] A. Shchepetov *et al.*, «Oblique modes effect on terahertz plasma wave resonant detection in InGaAs⁄InAlAs multichannel transistors», *Appl. Phys. Lett.*, vol. 92, n.º 24, p. 242105, jun. 2008, doi: 10.1063/1.2945286.

[7] W. Knap *et al.*, «Field Effect Transistors for Terahertz Detection: Physics and First Imaging Applications», *J Infrared Milli Terahz Waves*, ago. 2009, doi: 10.1007/s10762-009-9564-9.

[8] J. D. Sun, Y. F. Sun, D. M. Wu, Y. Cai, H. Qin, y B. S. Zhang, «High-responsivity, low-noise, room-temperature, self-mixing terahertz detector realized using floating antennas on a GaN-based field-effect transistor», *Appl. Phys. Lett.*, vol. 100, n.º 1, p. 013506, ene. 2012, doi: 10.1063/1.3673617.

[9] S. Boppel *et al.*, «CMOS Integrated Antenna-Coupled Field-Effect Transistors for the Detection of Radiation From 0.2 to 4.3 THz», *IEEE Trans. Microwave Theory Techn.*, vol. 60, n.º 12, pp. 3834-3843, dic. 2012, doi: 10.1109/TMTT.2012.2221732.

[10] J. Mateos y T. Gonzalez, «Plasma Enhanced Terahertz Rectification and Noise in InGaAs HEMTs», *IEEE Trans. THz Sci. Technol.*, vol. 2, n.º 5, pp. 562-569, sep. 2012, doi: 10.1109/TTHZ.2012.2209970.

[11] T. Watanabe *et al.*, «InP- and GaAs-Based Plasmonic High-Electron-Mobility Transistors for Room-Temperature Ultrahigh-Sensitive Terahertz Sensing and Imaging», *IEEE Sensors J.*, vol. 13, n.º 1, pp. 89-99, ene. 2013, doi: 10.1109/JSEN.2012.2225831.

[12] E. L. Ivchenko, «Effect of carrier heating on photovoltage in FET», *Phys. Solid State*, vol. 56, n.º 12, pp. 2514-2518, dic. 2014, doi: 10.1134/S1063783414120142.

[13] M. Bauer *et al.*, «Optimization of the Design of Terahertz Detectors Based on Si CMOS and AlGaN/GaN Field-Effect Transistors», *Int. J. Hi. Spe. Ele. Syst.*, vol. 25, n.º 03n04, p. 1640013, sep. 2016, doi: 10.1142/S0129156416400139.

[14] Z. Kargar, T. Linn, D. Ruic, y C. Jungemann, «Investigation of Transport Modeling for Plasma Waves in THz Devices», *IEEE Trans. Electron Devices*, vol. 63, n.º 11, pp. 4402-4408, nov. 2016, doi: 10.1109/TED.2016.2608422.

[15] C. Jungemann, T. Linn, K. Bittner, y H.-G. Brachtendorf, «Numerical investigation of plasma effects in silicon MOSFETs for THz-wave detection», *Solid-State Electronics*, vol. 128, pp. 129-134, feb. 2017, doi: 10.1016/j.sse.2016.10.030.

[16] M. Bauer *et al.*, «A High-Sensitivity AlGaN/GaN HEMT Terahertz Detector With Integrated Broadband Bow-Tie Antenna», *IEEE Trans. THz Sci. Technol.*, vol. 9, n.º 4, pp. 430-444, jul. 2019, doi: 10.1109/TTHZ.2019.2917782.

[17] Y. Li *et al.*, «GaN Schottky Barrier Diode-Based Wideband and Medium-Power Microwave Rectifier for Wireless Power Transmission», *IEEE Trans. Electron Devices*, vol. 67, n.º 10, pp. 4123-4129, oct. 2020, doi: 10.1109/TED.2020.3016619.

[18] W. Stillman, M. S. Shur, D. Veksler, S. Rumyantsev, y F. Guarin, «Device loading effects on nonresonant detection of terahertz radiation by silicon MOSFETs», *Electron. Lett.*, vol. 43, n.º 7, p. 422, 2007, doi: 10.1049/el:20073475.

[19] H. W. Hou, Z. Liu, J. H. Teng, T. Palacios, y S. J. Chua, «High Temperature Terahertz Detectors Realized by a GaN High Electron Mobility Transistor», *Sci Rep*, vol. 7, n.º 1, p. 46664, may 2017, doi: 10.1038/srep46664.

[20] E. Öjefors, A. Lisauskas, D. Glaab, H. G. Roskos, y U. R. Pfeiffer, «Terahertz Imaging Detectors in CMOS Technology», *J Infrared Milli Terahz Waves*, ago. 2009, doi: 10.1007/s10762-009-9569-4.

[21] M. Sakowicz *et al.*, «Terahertz responsivity of field effect transistors versus their static channel conductivity and loading effects», *Journal*

of Applied Physics, vol. 110, n.º 5, p. 054512, sep. 2011, doi: 10.1063/1.3632058.

[22] E. Ojefors, U. R. Pfeiffer, A. Lisauskas, y H. G. Roskos, «A 0.65 THz Focal-Plane Array in a Quarter-Micron CMOS Process Technology», *IEEE J. Solid-State Circuits*, vol. 44, n.º 7, pp. 1968-1976, jul. 2009, doi: 10.1109/JSSC.2009.2021911.

[23] A. Lisauskas, U. Pfeiffer, E. Öjefors, P. H. Bolìvar, D. Glaab, y H. G. Roskos, «Rational design of high-responsivity detectors of terahertz radiation based on distributed self-mixing in silicon field-effect transistors», *Journal of Applied Physics*, vol. 105, n.º 11, p. 114511, jun. 2009, doi: 10.1063/1.3140611.

[24] H. Kojima y T. Asano, «Impact of subthreshold slope on sensitivity of square law detector for high frequency radio wave detection», *Jpn. J. Appl. Phys.*, vol. 58, n.º SB, p. SBBL05, abr. 2019, doi: 10.7567/1347-4065/ab0275.

[25] H. Kojima *et al.*, «Analysis of square-law detector for high-sensitive detection of terahertz waves», *Journal of Applied Physics*, vol. 125, n.º 17, p. 174506, may 2019, doi: 10.1063/1.5083654.

[26] W. Knap *et al.*, «Nonresonant detection of terahertz radiation in field effect transistors», *Journal of Applied Physics*, vol. 91, n.º 11, pp. 9346-9353, jun. 2002, doi: 10.1063/1.1468257.

[27] M. A. Andersson y J. Stake, «An Accurate Empirical Model Based on Volterra Series for FET Power Detectors», *IEEE Trans. Microwave Theory Techn.*, vol. 64, n.º 5, pp. 1431-1441, may 2016, doi: 10.1109/TMTT.2016.2532326.

[28] A. M. Cowley y H. O. Sorensen, «Quantitative Comparison of Solid-State Microwave Detectors», *IEEE Trans. Microwave Theory Techn.*, vol. 14, n.º 12, pp. 588-602, dic. 1966, doi: 10.1109/TMTT.1966.1126337.

[29] P. Altuntas *et al.*, «Power Performance at 40 GHz of AlGaN/GaN High-Electron Mobility Transistors Grown by Molecular Beam Epitaxy on Si(111) Substrate», *IEEE Electron Device Lett.*, vol. 36, n.º 4, pp. 303-305, abr. 2015, doi: 10.1109/LED.2015.2404358.

[30] S. Rennesson *et al.*, «Optimization of $Al_{0.29}Ga_{0.71}N$/GaN High Electron Mobility Heterostructures for High-Power/Frequency Performances », *IEEE Trans. Electron Devices*, vol. 60, n.º 10, pp. 3105-3111, oct. 2013, doi: 10.1109/TED.2013.2272334.

[31] H. Sánchez-Martín, I. Íñiguez-de-la-Torre, S. García-Sánchez, J. Mateos, y T. González, «Monte Carlo analysis of thermal effects in the DC and AC performance of AlGaN/GaN HEMTs», *Solid-State Electronics*, vol. 193, p. 108289, jul. 2022, doi: 10.1016/j.sse.2022.108289.

[32] J. Pedro, J. Gomes, y L. Nunes, «Electro-Thermal and Trapping Characterization of AlGaN/GaN RF Power HEMTs», en *2021 IEEE BiCMOS and Compound Semiconductor Integrated Circuits and Technology Symposium (BCICTS)*, Monterey, CA, USA, dic. 2021, pp. 1-6. doi: 10.1109/BCICTS50416.2021.9682206.

[33] A. Santarelli *et al.*, «A Double-Pulse Technique for the Dynamic I/V Characterization of GaN FETs», *IEEE Microw. Wireless Compon. Lett.*, vol. 24, n.º 2, pp. 132-134, feb. 2014, doi: 10.1109/LMWC.2013.2290216.

[34] A. Santarelli *et al.*, «Nonquasi-static large-signal model of GaN FETs through an equivalent voltage approach», *Int J RF and Microwave Comp Aid Eng*, vol. 18, n.º 6, pp. 507-516, nov. 2008, doi: 10.1002/mmce.20326.

[35] E. Pérez-Martín *et al.*, «Trap-related frequency dispersion of zero-bias microwave responsivity at low temperature in GaN-based self-switching diodes», *Nanotechnology*, vol. 31, n.º 40, p. 405204, oct. 2020, doi: 10.1088/1361-6528/ab9d44.

[36] H. Sánchez-Martín *et al.*, «Anomalous DC and RF behavior of virgin AlGaN/AlN/GaN HEMTs», *Semicond. Sci. Technol.*, vol. 32, n.º 3, p. 035011, mar. 2017, doi: 10.1088/1361-6641/aa5473.

[37] G. Paz-Martínez *et al.*, «Temperature and Gate-Length Dependence of Subthreshold RF Detection in GaN HEMTs», *Sensors*, vol. 22, n.º 4, p. 1515, feb. 2022, doi: 10.3390/s22041515.

[38] B. Sun, «Does GaN Have a Body Diode?-Understanding the Third Quadrant Operation of GaN», *Application Report SNOAA36; Texas Instruments*, p. 7, 2019.

[39] T. Yasui, R. Ishikawa, y K. Honjo, «GaN HEMT DC I – V Device Model for Accurate RF Rectifier Simulation», *IEEE Microw. Wireless Compon. Lett.*, vol. 27, n.º 10, pp. 930-932, oct. 2017, doi: 10.1109/LMWC.2017.2746678.

[40] C. Balocco *et al.*, «Room-temperature operation of a unipolar nanodiode at terahertz frequencies», *Appl. Phys. Lett.*, vol. 98, n.º 22, p. 223501, may 2011, doi: 10.1063/1.3595414.

[41] S. R. Kasjoo y A. M. Song, «Terahertz Detection Using Nanorectifiers», *IEEE Electron Device Lett.*, vol. 34, n.º 12, pp. 1554-1556, dic. 2013, doi: 10.1109/LED.2013.2285162.

[42] M. I. W. Khan, S. Kim, D.-W. Park, H.-J. Kim, S.-K. Han, y S.-G. Lee, «Nonlinear Analysis of Nonresonant THz Response of MOSFET and Implementation of a High-Responsivity Cross-Coupled THz Detector», *IEEE Trans. THz Sci. Technol.*, vol. 8, n.º 1, pp. 108-120, ene. 2018, doi: 10.1109/TTHZ.2017.2778499.

[43] G. Paz-Martínez *et al.*, «Comparison of GaN and InGaAs high electron mobility transistors as zero-bias microwave detectors», *Journal of Applied Physics*, vol. 132, n.º 13, p. 134501, oct. 2022, doi: 10.1063/5.0111114.